Hindawi
International Journal of Antennas and Propagation
Volume 2023, Article ID 5184139, 10 pages
https://doi.org/10.1155/2023/5184139

Research Article

Single-Layer Differential-Fed Wideband Metasurface Antenna Using Characteristic Mode Analysis

Chao Huang, Chen-Jiang Guo, Yi Yuan, Xia Ma, and Jun Ding

School of Electronics and Information, Northwestern Polytechnical University, Xi'an 710072, China

Correspondence should be addressed to Chao Huang; huangchaoxidian@163.com

Received 8 June 2023; Revised 17 August 2023; Accepted 30 October 2023; Published 11 November 2023

Academic Editor: Truong Khang Nguyen

Copyright © 2023 Chao Huang et al. This is an open access article distributed under the Creative Commons Attribution License, which permits unrestricted use, distribution, and reproduction in any medium, provided the original work is properly cited.

A single-layer differential-fed (DF) wideband metasurface (MTS) antenna is proposed in this paper. As the prototype, a three-by-three MTS formed by identical rectangular patches is investigated at first. We observe that there are many unwanted higher-order modes (HOMs) resonating near the wanted fundamental mode. Two probes with differential signals feed MTS on its centerline to suppress the majority of HOMs. The remaining HOM can be removed from the discussed frequency range by modifying the prototype MTS to a nonuniform structure. Then, the optimal feeding positions (FPs) are determined by a quantitative prediction of the impendence bandwidth (IBW) without any physical feeds involved. The processes of HOMs suppression and FPs determination are based on characteristic mode analysis with the virtual probes. Moreover, two interdigital capacitor plates are loaded on the probes to improve the impedance matching of the antenna. Finally, the proposed DF MTS antenna is fabricated and measured. The measured −10-dB IBW is 18.4% (4.93 to 5.93 GHz) with broadside radiation, stable high gains, and front-to-back ratios better than 21 dB.

1. Introduction

Differential circuits with the advantages of low noise, harmonic suppression, high linearity, and large dynamic range have been widely applied in radio frequency (RF) integrated circuits and microwave monolithic integrated circuits [1]. To match the differential circuit, various types of differential-fed (DF) antennas, especially DF microstrip patch antennas (MPAs) [2–4], were presented. However, low-profile MPAs usually suffer from narrow impedance bandwidth (IBW) and low gains.

Metasurface (MTS), a two-dimensional form of metamaterial, has rich potential for manipulating electromagnetic waves [5, 6]. As a combination with antennas, MTS antennas have been widely employed to enhance IBW and the gains of MPAs. Compared with MPAs, the resonating modes have a denser distribution for MTS, showing an opportunity in mode combination and a challenge in mode suppression. Therefore, MTS is usually coupled fed by sources with fixed polarization to suppress unwanted orthogonal modes. In [7–9], MTSs are coupled fed by y- or x-polarized slot antennas, and a wider IBW can be achieved by combining a slot mode and MTS modes. However, these antennas usually suffer from lower front-to-back ratios (FBRs) for the bidirectional radiation of slots. To reduce the backward radiation, coupled patches and L-probes are employed to feed MTSs [10–13]. Nevertheless, the configurations of these antennas are always complex. In [14], MTS is fed by an aperture coupling through a short-end coplanar waveguide (CPW). The antenna achieves broadband performance with a simple single-layer structure. Still, it exhibits poor FBRs and distorted radiation patterns. In summary, the above feeding methods cannot simultaneously realize an MTS antenna with broadband, good radiation characteristics, and single-layer configurations.

To investigate the operating mechanism of MTS antennas, various analyzing methods were presented, including the equivalent circuit method [7], reflection coefficients calculation [9], and effective medium theory [15]. Compared with the above methods, the characteristic mode analysis (CMA) shows superiority in characterizing the modal resonant behavior of arbitrarily shaped objects,

especially for analyzing nonuniform MTS or small-scale MTS [16, 17].

In this paper, we propose a DF MTS antenna with a single-layer configuration. The design begins with analyzing the intrinsic properties of a uniform three-by-three MTS with rectangular patches, and its higher-order modes (HOMs) with unwanted radiation features are found to resonate near the fundamental broadside mode. By observing the modal E-fields of HOMs, it is possible to suppress most of them by symmetrically arranging two DF probes on the centerline of MTS. The resonating frequency of the remaining HOM can be removed from the discussed range by reducing the length of side patches in MTS. Then, a quantitative prediction of IBW is utilized to determine the optimal feeding positions (FPs). The suppression of HOMs and determination of FPs are all based on source-free CMA with a method of virtual probes, which is easier to understand and more time-saving than the traditional physical port simulation. Moreover, two interdigital capacitor plates (ICPs) are loaded on the DF probes to compensate for the probe inductances and improve IBW. Since no slot modes or HOMs are excited, the proposed antenna exhibits stable broadside radiation with high FBRs in the operating band.

This paper is organized as follows. Section 2 presents the basic theory of CMA and a differential impedance analysis method based on virtual probes, which provides the theoretical basis for the proposed design. Section 3 shows the geometry and working mechanism of the proposed antenna, including the suppression of HOMs, the determination of FPs, and the improvement of IBW. The measured results of the proposed antenna are presented and discussed in Section 4, and we draw the conclusions in Section 5.

2. CMA and Differential Impedance with Virtual Probes

2.1. Theory of CMA. In characteristic mode (CM) theory, the modal resonant behavior of objects in arbitrary shapes can be characterized by their generalized eigenvalue equations as follows [18]:

$$\mathbf{X}\mathbf{J}_n = \lambda_n \mathbf{R}\mathbf{J}_n, \tag{1}$$

where $\mathbf{J}_n$ is the eigenvector, λ_n is the eigenvalue, and subscript n denotes the index number of CMs. The parameters $\mathbf{X}$ and $\mathbf{R}$ are the real and imaginary parts of the impedance matrix, respectively. The eigenvalue λ_n has a significant physical meaning, whose magnitude can reflect the total stored field energy within a radiation or scattering problem. However, since λ_n has a large value range of $[-\infty, +\infty]$, researchers often replace it with the modal significance (MS) as follows [19]:

$$\mathrm{MS} = \left|\frac{1}{1 + j\lambda_n}\right|. \tag{2}$$

The value range of MS is [0, 1], which is more convenient for observation. A frequency with $\mathrm{MS} = 1$ is the resonant frequency of a mode, and a mode can be regarded as the dominant mode when its $\mathrm{MS} \geq 0.7$.

2.2. Differential Impedance with Virtual Probes. Differential impendence Z_{dd} is an essential parameter for DF antennas, which can be calculated by

$$Z_{dd} = (Z_{11} - Z_{12}) + (Z_{22} - Z_{21}), \tag{3}$$

where $Z_{11/22}$ and $Z_{12/21}$ are the self- and mutual impedances, respectively. For a DF planar antenna shown in Figure 1, referring to the method in [20], its physical probes can be equivalent to two virtual probes in the impedance analysis. The virtual probe is an idealized model that disregards the physical dimensions of the probe and treats it as a uniform current filament. By introducing the concept of "virtual probe," $Z_{11/22}$ and $Z_{12/21}$ in (3) can be written as follows [21]:

$$Z_{11/22} = -\frac{\iiint \mathbf{E}(r_{1/2}) \cdot \mathbf{J}_{1/2} \mathrm{dv}}{I_{1/2}^2}, \tag{4}$$

$$Z_{12/21} = -\frac{\iiint \mathbf{E}(r_{1/2}) \cdot \mathbf{J}_{2/1} \mathrm{dv}}{I_1 I_2}, \tag{5}$$

$$I_{1/2} = \iint \mathbf{J}_{1/2} \cdot \hat{z} \mathrm{dS}, \tag{6}$$

$$\mathbf{J}_{1/2} = \hat{z}\delta(x - x_{1/2}, y - y_{1/2}) \quad 0 \leq z \leq h, \tag{7}$$

where $\mathbf{E}(r_{1/2})$, $\mathbf{J}_{1/2}$, and $I_{1/2}$ are the total E-fields, the excitation current densities, and the excitation currents at FPs $r_{1/2}(x_{1/2}, y_{1/2}, h)$, respectively. According to the theory of CM, $\mathbf{E}(r_{1/2})$ can be expanded using a set of orthogonal modal E-fields $\mathbf{E}_n(r_{1/2})$ as

$$\mathbf{E}(r_{1/2}) = \sum_n \frac{\iiint \mathbf{E}_n(r_{1/2}) \cdot \mathbf{J}_{1/2} \mathrm{dv}}{1 + j\lambda_n} \mathbf{E}_n(r_{1/2}). \tag{8}$$

Assuming the vertical components of $\mathbf{E}_n(r_{1/2})$ are uniform underneath the radiator and substituting (6)–(8) into (4) and (5), the self- and mutual impedances can be simplified as follows [3]:

$$Z_{11/22} = -\sum_n \frac{E_n^z(r_{1/2})h}{1 + j\lambda_n} E_n^z(r_{1/2})h, \tag{9}$$

$$Z_{12/21} = -\sum_n \frac{E_n^z(r_1)h}{1 + j\lambda_n} E_n^z(r_2)h, \tag{10}$$

where $E_n^z(r_{1/2})$ are the imaginary part of the z-component of $\mathbf{E}_n(r_{1/2})$. Substituting (9) and (10) into (3), the differential impendence with the virtual probes can be expressed as

$$Z_{dd} = \sum_n Z_{dd,n} = -\sum_n \frac{h^2}{1 + j\lambda_n} [E_n^z(r_1) - E_n^z(r_2)]^2, \tag{11}$$

where $Z_{dd,n}$ is the differential impendence of each mode.

However, since (11) is derived based on the virtual probes, it neglects the inductances contributed by the physical probes. Furthermore, to ensure the antenna presents an open circuit at dc, an equivalent dc capacitance C_{dc} should be introduced [22]. Taking into account of the probe

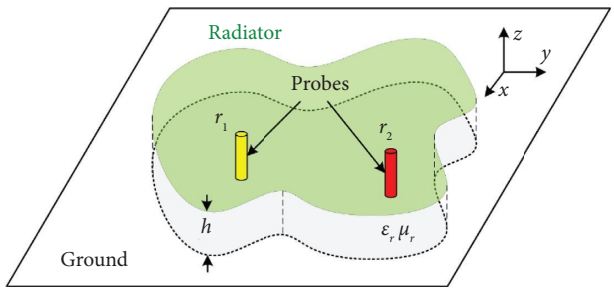

FIGURE 1: Schematic of an arbitrary planar antenna fed by DF probes at r_1 and r_2.

inductances and the dc capacitance, the differential impendence in (11) can be rewritten as

$$Z_{\mathrm{dd}} = \frac{1}{j\omega C_{\mathrm{dc}}} + 2j\omega\left(L_{\mathrm{self}} - M\right) + \sum_n Z_{dd,n}, \tag{12}$$

where L_{self} and M are the self- and mutual inductances, respectively, expressed as follows [23]:

$$L_{\mathrm{self}} = \frac{\mu_0}{2\pi} l \left[\ln\left(\frac{l}{\rho} + \sqrt{1 + \left(\frac{l}{\rho}\right)^2} \right) - \sqrt{1 + \left(\frac{\rho}{l}\right)^2} + \frac{\rho}{l} + \frac{1}{4} \right], \tag{13}$$

$$M = \frac{\mu_0}{2\pi} l \left[\ln\left(\frac{l}{D} + \sqrt{1 + \left(\frac{l}{D}\right)^2} \right) - \sqrt{1 + \left(\frac{D}{l}\right)^2} + \frac{D}{l} \right], \tag{14}$$

where l is the length, ρ is the radius of the probes, and D is the distance between the two probes. Furthermore, the differential reflection coefficient S_{dd} of the antenna can also be derived from Z_{dd} in (12) as follows [24]:

$$S_{dd} = \frac{Z_{dd} - Z_c}{Z_{dd} + Z_c}, \tag{15}$$

where the characteristic impedance Z_c is 100 Ω for the differential port.

In this paper, $E_n^z(r_{1/2})$ and λ_n of each mode for MTS can be obtained by source-free CMA simulations performed in FEKO. The values of L_{self} and M are determined by (13) and (14) with the parameters of the physical probes, and the length of the probes is equal to the height of the substrate h. The dc capacitance C_{dc} is calculated in Ansys Maxwell using the finite element method.

3. Antenna Design and Operating Mechanism

3.1. Antenna Geometry. The configuration of the proposed DF MTS antenna is shown in Figure 2. From the side view, an MTS and a ground plane are etched on the two sides of an F4B220M substrate ($\varepsilon_r = 2.2$ and $\tan\sigma = 0.0009$) with a thickness of h, respectively. From the top view, the MTS features a nonuniform structure formed by nine rectangular metallic patches. The dimensions of the middle and the two side patches of MTS are $L_1 \times W_m$ and $L_2 \times W_m$, respectively. The distances between adjacent patches are denoted by g. In order to excite MTS, two DF probes with a radius of R_1 are symmetrically arranged on its centerline (AA′) at positions of (0 mm, ±18 mm, z). From the enlarged view, two ICPs with an outer radius of R_2 are loaded on the two probes for better impendence matching. The eight fingers with dimensions of $L_f \times W_f$ have a gap width of G_1 with ICP.

3.2. Suppression of HOMs. The design starts with a three-by-three MTS with identical rectangular patches (MTS 1) (see Figure 3(a)), and its MSs and corresponding radiation patterns of the dominant modes ($\mathbf{J}_1$–$\mathbf{J}_8$) in the range of 4 to 7 GHz are depicted in Figures 3(b) and 3(c), respectively. As can be seen, modes $\mathbf{J}_2$–$\mathbf{J}_5$, $\mathbf{J}_7$, and $\mathbf{J}_8$ feature radiation nulls at the boresight are unwanted modes that should be suppressed in the design. Although both modes $\mathbf{J}_1$ and $\mathbf{J}_6$ can generate broadside radiation patterns, only $\mathbf{J}_1$ should be excited as $\mathbf{J}_6$ is an x-polarized mode. According to (11), the $Z_{dd,n}$ of a mode has little contribution to the total differential impendence (Z_{dd}) when its modal E-fields are identical in magnitude and phase under the two differential ports, i.e., $E_n^z(r_1) = E_n^z(r_2)$, which also means the mode can be suppressed effectively.

Figure 4 plots the z-component modal E-fields of $\mathbf{J}_1$–$\mathbf{J}_8$ under the centerline (AA′) of MTS 1 at 5.5 GHz. It is found that only $\mathbf{J}_1$ and $\mathbf{J}_5$ in odd-symmetrical E-field distributions can be excited with differential feeds. The other modes in zero-magnitude ($\mathbf{J}_2$, $\mathbf{J}_4$, $\mathbf{J}_6$, and $\mathbf{J}_7$) and even-symmetrical ($\mathbf{J}_3$ and $\mathbf{J}_8$) distributions can be suppressed successfully.

In order to further suppress $\mathbf{J}_5$, the modal currents of $\mathbf{J}_1$ and $\mathbf{J}_5$ are investigated (see Figure 5(a)). Compared with $\mathbf{J}_1$, the modal currents of $\mathbf{J}_5$ mainly distribute on the right and left sides of MTS 1. Therefore, if the length of side patches L_2 is reduced, the resonating frequency of $\mathbf{J}_5$ will move away from the range of 4 to 7 GHz, and the effect of $\mathbf{J}_5$ will be reduced. Figure 5(b) shows MSs of $\mathbf{J}_5$ with different L_2. As L_2 decreases from 13 to 10 mm, $\mathbf{J}_5$ has a remarkable blue shift from 6.35 to 7.8 GHz.

To suppress $\mathbf{J}_5$, a modified MTS (MTS 2) with $L_2 = 10$ mm (see Figure 6(a)) is selected for the following design, and its MSs and corresponding radiation patterns for the dominant modes ($\mathbf{J}_1$'–$\mathbf{J}_6$') are depicted in Figures 6(b) and 6(c), respectively. Compared with MTS 1, MTS 2 has less unwanted HOMs ($\mathbf{J}_2$'–$\mathbf{J}_6$'). By observing the z-component modal E-fields of MTS 2 in Figure 7, only the wanted mode $\mathbf{J}_1$' with broadside radiation and odd-symmetrical E-field distributions can be excited when differential probes feed MTS 2. The expression of Z_{dd} for the MTS 2-based DF antenna can be derived from (12) as

$$Z_{dd} = \frac{1}{j\omega C_{\mathrm{dc}}} + 2j\omega\left(L_{\mathrm{self}} - M\right) + Z_{dd,1'}. \tag{16}$$

3.3. Determination of FPs. After suppressing all unwanted HOMs of MTS, the FPs need to be further optimized for a wider IBW. According to (6), the bandwidth of each feeding point on the centerline of MTS 2 can be predicted by

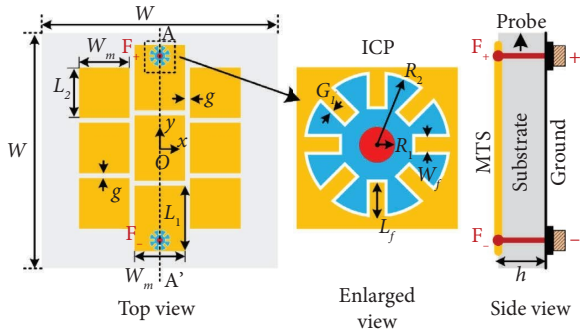

FIGURE 2: Configuration of the proposed MTS antenna. $L_1 = 13$ mm, $L_2 = 10$ mm, $L_f = 1$ mm, $W = 60$ mm, $W_m = 10$ mm, $W_f = 0.42$ mm, $g = 1$ mm, $G_1 = 0.1$ mm, $R_1 = 0.5$ mm, $R_2 = 2$ mm, $h = 3$ mm.

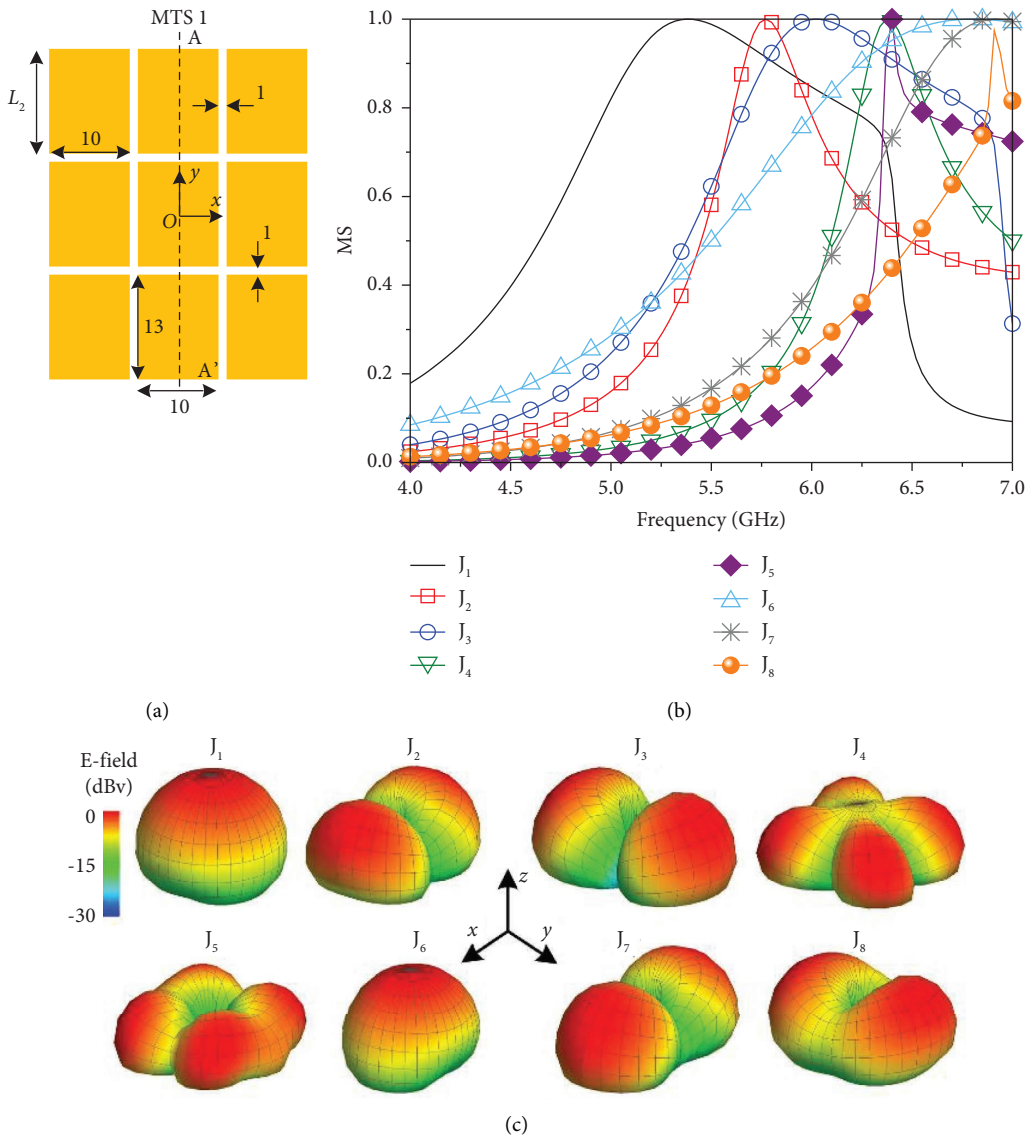

FIGURE 3: Geometry and CMA results of MTS 1. (a) Geometry (units: mm). (b) MSs and (c) corresponding radiation patterns of the dominant modes for MTS 1 at 5.5 GHz.

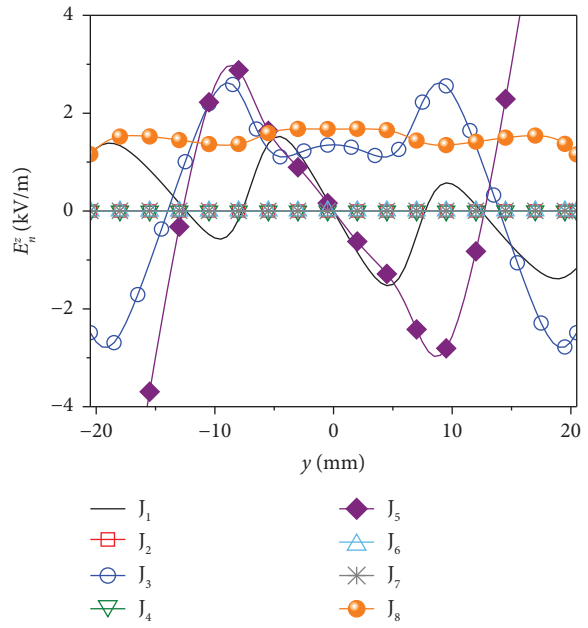

FIGURE 4: E_n^z under the centerline of MTS 1 at 5.5 GHz.

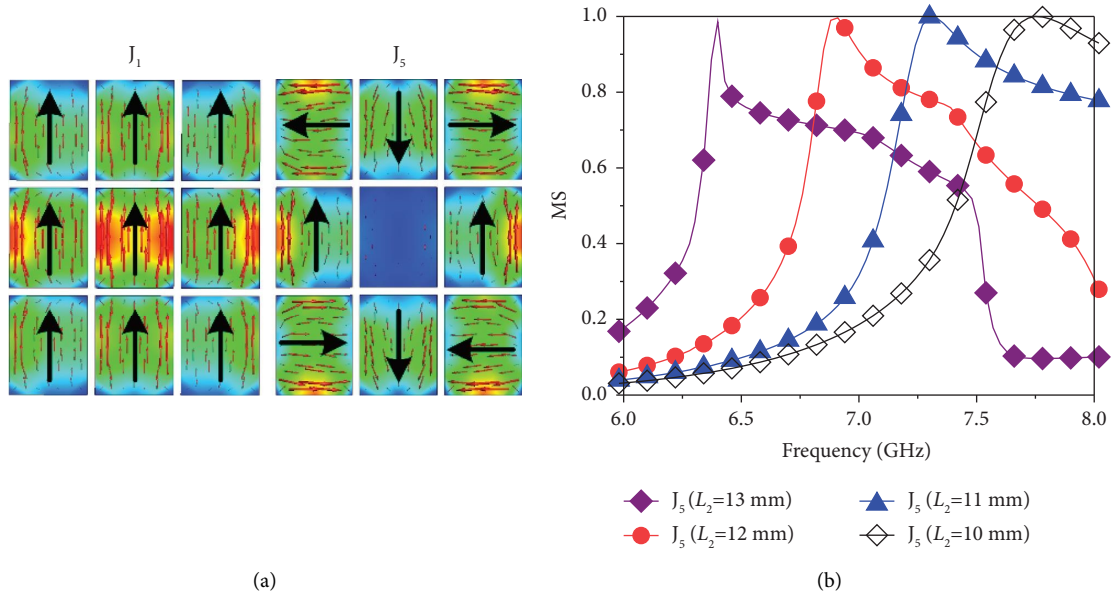

FIGURE 5: Modal currents of $\mathbf{J}_1$ and $\mathbf{J}_5$, and MSs of $\mathbf{J}_5$ with different L_2. (a) Modal currents at 5.5 GHz. (b) MSs.

calculating its S_{dd} values in the entire operating band. The prediction is based on the method of virtual probes in Section 2, and the corresponding C_{dc} is estimated as 1.35 pF. The points with y-coordinate values varying from ±2 to ±20 mm (±0.5 mm step) are selected. The IBW values ($|S_{dd}| < -10$ dB) of these points calculated with the virtual probes are illustrated in Figure 8(a) (upper bars), and the corresponding results simulated with the physical probes performed in Ansys HFSS (lower bars) are also given for verification. The upper and lower bars have similar trends and values, and both of them illustrate an optimized IBW (about 450 MHz) can be obtained when the probes are fed near the positions of (0 mm, ±18 mm, z). Figure 8(b) shows Z_{dd} curves of MTS 2 with virtual and physical feeds at (0 mm, ±18 mm, z). The imaginary parts of Z_{dd} show positive values in the operating band, mainly induced by the self- and mutual inductances of probes.

3.4. Improvement of Impedance Matching. In order to compensate for the probe inductances, two circular capacitor plates (CCPs) are loaded on the probes at first for IBW improvement. The CCP (see Figure 9(a)) has been widely applied to enhance the IBW of probe-fed patch

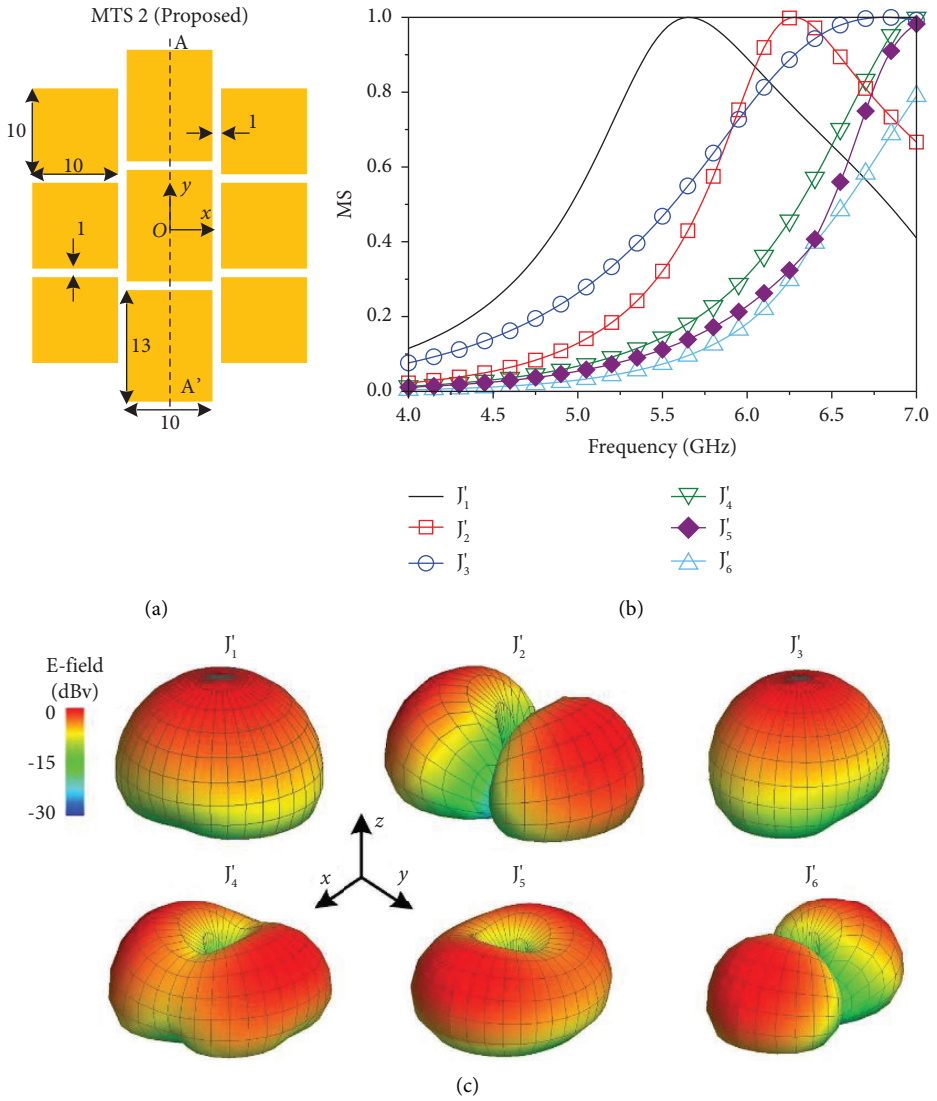

Figure 6: Geometry and CMA results of MTS 2. (a) Geometry (unit: mm). (b) MSs and (c) corresponding radiation patterns of the dominant modes for MTS 1 at 5.5 GHz.

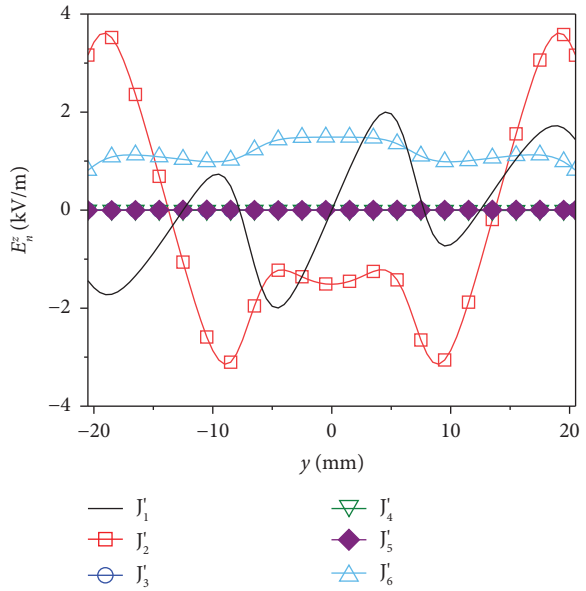

Figure 7: E_n^z under the centerline of MTS 2 at 5.5 GHz.

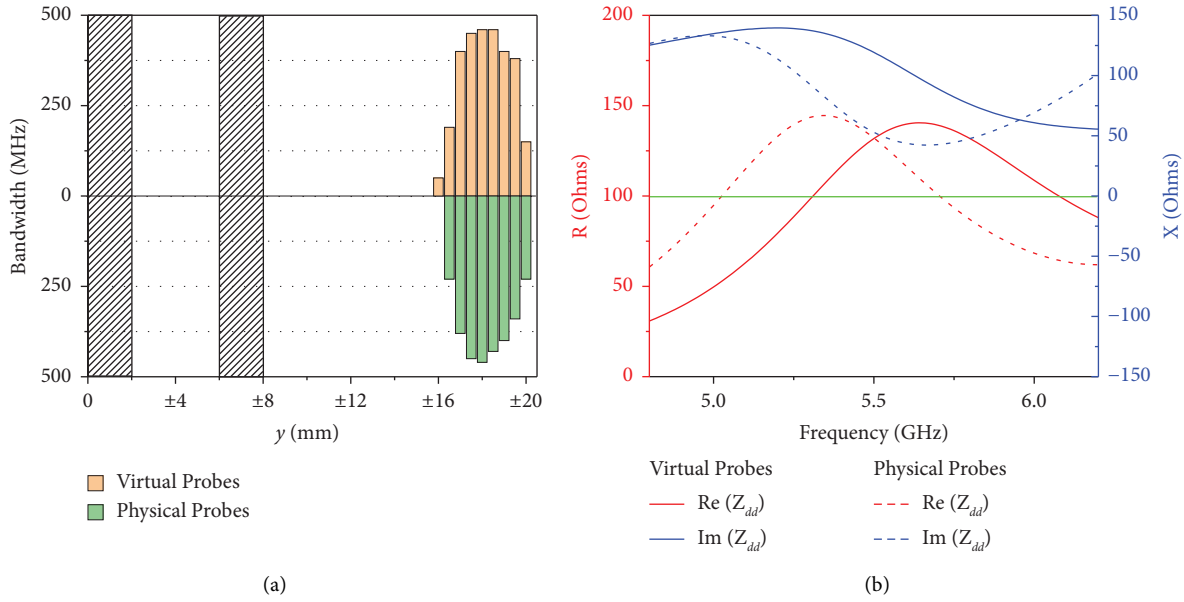

FIGURE 8: IBW and Z_{dd} results with virtual and physical probes. (a) IBW values at positions on the centerline of MTS 2. (b) Z_{dd} curves of MTS 2 with feeds at (0 mm, ±18 mm, z).

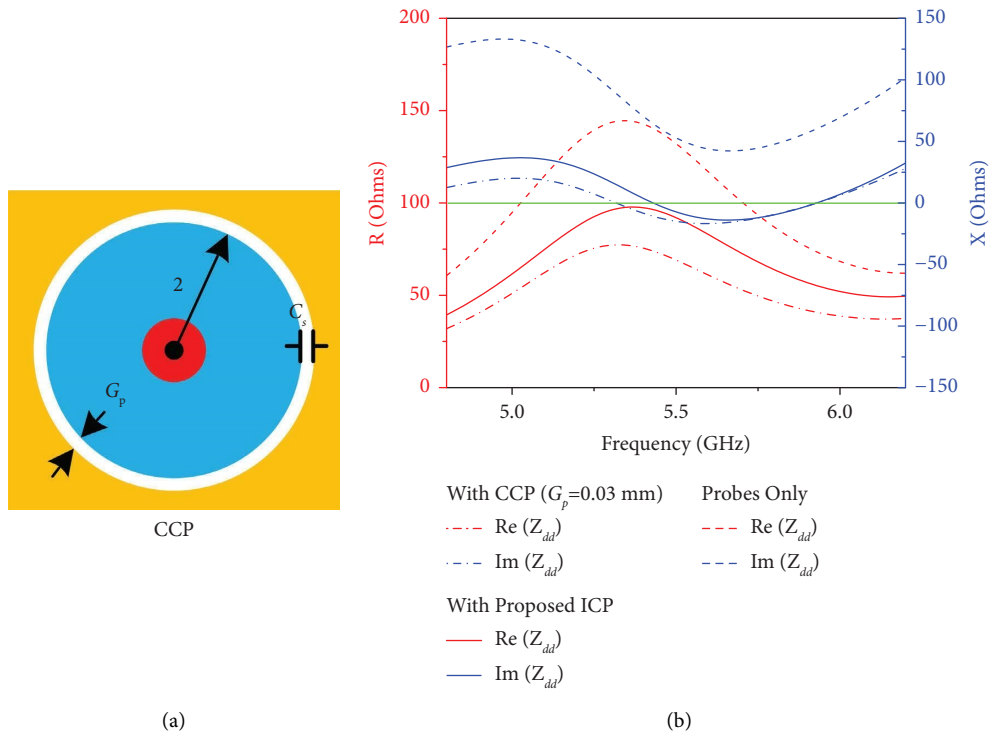

FIGURE 9: Geometry of CCP and simulated Z_{dd} of MTS 2 with different feeds at (0 mm, ±18 mm, z). (a) Geometry. (b) Z_{dd} curves.

antennas with a thick substrate because it can introduce a series radial capacitor C_s [25]. The radius of CCP is set to 2 mm (slightly less than h) for larger C_s while weakening the effect of its TEM mode [26]. From Figure 8(b), the imaginary part of Z_{dd} is $j85\,\Omega$ at 5.35 GHz for the physical probe simulation, and the required value of C_s is 0.7 pF. Then, the corresponding radial gap width G_p can be calculated using the equations in [26] as 0.03 mm, which is narrow and sensitive to the dimensional errors in fabrication. Because the interdigital capacitor has a greater capacitance than the gap capacitor in the same size, the final design adjusts the CCPs to ICPs with an interdigital gap width (G_1) of 0.1 mm. Figure 9(b) shows the simulated Z_{dd} results of MTS 2 fed by the nonloaded, the CCP-loaded, and the proposed ICP-

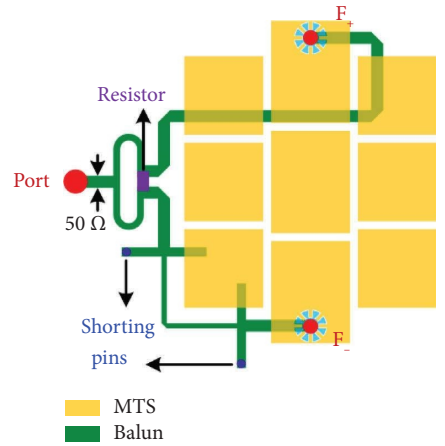

Figure 10: Top view of the proposed DF MTS antenna with the balun.

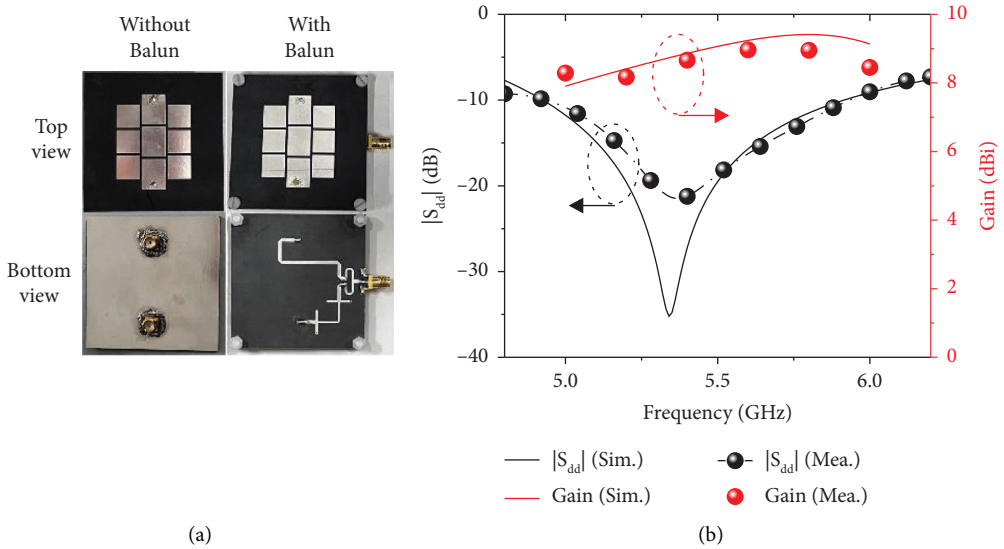

Figure 11: Simulated and measured $|S_{dd}|$ and gains, and the photographs of the proposed DF MTS antenna. (a) Photographs. (b) $|S_{dd}|$ and gains.

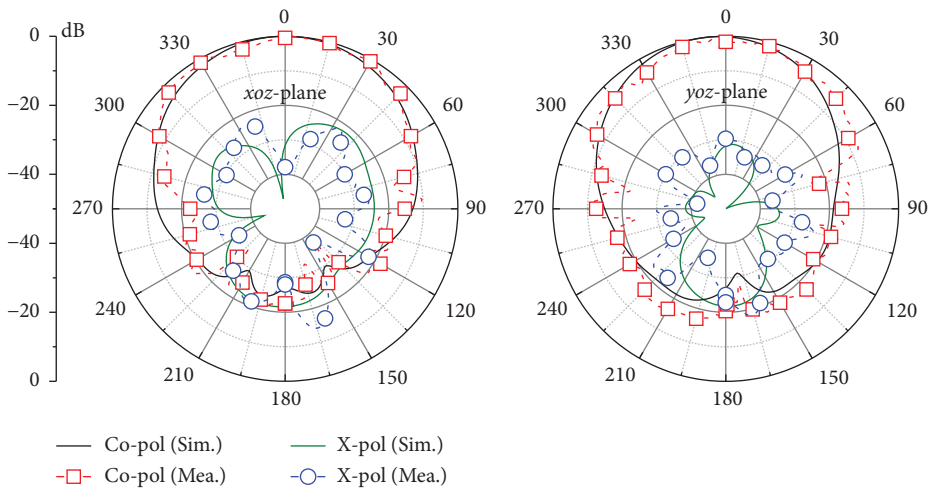

Figure 12: Simulated and measured normalized patterns of the proposed DF MTS antenna at 5.35 GHz.

Table 1: Comparisons with other broadside wideband MTS antennas.

Reference	Number of layers	Feeds	IBW (%)	FBR (dB)	Peak gain (dBi)
[11]	3	Patch	20.5	>20	8.6
[12]	3	L-probes	20.2	>15	8.1
[8]	2	Slot	79	>9	8.6
[14]	1	CPW slot	67.3	>8	9.18
Our work	1	DF probes	18.4	>21	8.96

loaded probes at (0 mm, ±18 mm, z). This figure illustrates ICP with $G_1 = 0.1$ mm has a similar effect as CCP with $G_p = 0.03$ mm in compensating for the imaginary part. Moreover, the real part with ICP loading is closer to 100 Ω at the resonant frequency, showing a better match with Z_c (100 Ω) than CCP loading.

4. Results and Discussion

The proposed DF antenna with the parameters in the caption of Figure 2 was fabricated, and its $|S_{dd}|$ results are calculated based on S-parameters measured by the vector network analyzer [27]. In order to facilitate far-field testing, the fabricated antenna is integrated with a wideband balun (see Figure 10). The balun referenced in [28] is etched on a 0.5-mm thick F4B220M substrate and shares the same ground plane with the proposed DF antenna. Figure 11(a) shows the photographs of the proposed antenna, and its measured and simulated $|S_{dd}|$ and gains are plotted in Figure 11(b). The measured results agree with the simulated ones, indicating that the proposed antenna can cover 4.93 to 5.93 GHz (18.4%) with reflection coefficients less than −10 dB and broadside gains varying from 8.17 to 8.96 dBi. Figure 12 shows the simulated and measured normalized radiation patterns of the proposed antenna at 5.35 GHz, showing broadside radiation with good polarization purity and a front-to-back ratio (FBR) better than 21 dB in both the *xoz*- and *yoz* planes.

Comparisons of the proposed antenna with the other reported wideband MTS antennas are tabulated in Table 1. With approaching IBW and FBR performances, the proposed antenna achieved a simpler structure than the works in [11, 12], making fabrication easier. Although antennas in [8, 14] exhibit a much broader IBW than our work, the introduction of slots and HOMs render them worse than the proposed antenna in the backward radiation and the pattern stability.

5. Conclusion

In this paper, a single-layer DF wideband MTS antenna with broadside radiation is proposed and discussed. The suppression of HOMs is achieved by adding differential feeds and reshaping the geometry of MTS. Unlike other reported designs with time-consuming full-wave simulations, the optimization of FPs in this study is based on an IBW prediction, which is more efficient. All the above processes use CMA with virtual rather than physical feeds. Moreover, the conventional CCP loading for the thick substrate is modified to the novel ICP loading, which can compensate for the probe inductances of the proposed antenna printed on a thin substrate. The proposed antenna has a simple structure and a low profile, which is easy to fabricate. Its measured results show an 18.4% IBW with an FBR greater than 21 dB. In addition, the proposed MTS antenna also presents stabilities in gains and radiation patterns in the entire operating band. Compared with other reported wideband MTS antennas, the proposed antenna can achieve broadband, good radiation characteristics, and single-layer configurations simultaneously, ensuring its potential applications in balanced RF systems.

Data Availability

All data, models, and code used to support the findings of this study are available from the corresponding author upon request.

Conflicts of Interest

The authors declare that they have no conflicts of interest.

References

[1] W. R. Eisenstadt, B. Stengel, and B. M. Thompson, *Microwave Differential Circuit Design Using Mixed-Mode S-Parameters*, Artech House, Boston, MA, USA, 2006.

[2] Y. F. Wang, F. G. Zhu, and S. Gao, "Design and investigation of differential-fed ultra-wideband patch antenna with polarization diversity," *International Journal of Antennas and Propagation*, vol. 2016, Article ID 6682038, 6 pages, 2016.

[3] J. F. Lin and L. Zhu, "Low-profile high-directivity circularly-polarized differential-fed patch antenna with characteristic modes analysis," *IEEE Transactions on Antennas and Propagation*, vol. 69, no. 2, pp. 723–733, 2021.

[4] T. H. Chen, Y. Y. Chen, and R. L. Jian, "A wideband differential-fed microstrip patch antenna based on radiation of three resonant modes," *International Journal of Antennas and Propagation*, vol. 2019, Article ID 4656141, 7 pages, 2019.

[5] S. J. Li, B. W. Han, Z. Y. Li et al., "Transmissive coding metasurface with dual-circularly polarized multi-beam," *Optics Express*, vol. 30, no. 15, pp. 26362–26376, 2022.

[6] S. J. Li, Z. Y. Li, X. B. Liu et al., "Transmissive digital coding metasurfaces for polarization-dependent dual-mode quad orbital angular momentum beams," *ACS Applied Materials & Interfaces*, vol. 15, no. 19, pp. 23690–23700, 2023.

[7] D. Chen, W. Yang, W. Che, and Q. Xue, "Miniaturized wideband metasurface antennas using cross-layer capacitive loading," *IEEE Antennas and Wireless Propagation Letters*, vol. 21, no. 1, pp. 19–23, 2022.

[8] S. Liu, D. Yang, Y. Chen, K. Sun, X. Zhang, and Y. Xiang, "Low-profile broadband metasurface antenna under multi-mode resonance," *IEEE Antennas and Wireless Propagation Letters*, vol. 20, no. 9, pp. 1696–1700, 2021.

[9] Y. F. Cheng, X. Ding, X. Xu, X. Zhong, and C. Liao, "Design and analysis of a bow-tie slot-coupled wideband metasurface antenna," *IEEE Antennas and Wireless Propagation Letters*, vol. 18, no. 7, pp. 1342–1346, 2019.

[10] G. Gao, R. F. Zhang, W. F. Geng, H. J. Meng, and B. Hu, "Characteristic mode analysis of a nonuniform metasurface antenna for wearable applications," *IEEE Antennas and Wireless Propagation Letters*, vol. 19, no. 8, pp. 1355–1359, 2020.

[11] W. K. Wan, M. Xue, L. Cao, T. C. Ye, and Q. D. Wang, "Low-profile compact metasurface-loaded patch antenna with enhanced bandwidth," *Microwave and Optical Technology Letters*, vol. 63, no. 10, pp. 2656–2661, 2021.

[12] J. Liu, Z. Weng, Z. Q. Zhang, Y. Qiu, Y. X. Zhang, and Y. C. Jiao, "A wideband pattern diversity antenna with a low profile based on metasurface," *IEEE Antennas and Wireless Propagation Letters*, vol. 20, no. 3, pp. 303–307, 2021.

[13] W. E. I. Liu, Z. N. Chen, and X. Qing, "Broadband low-profile L-probe fed metasurface antenna with TM leaky wave and TE surface wave resonances," *IEEE Transactions on Antennas and Propagation*, vol. 68, no. 3, pp. 1348–1355, 2020.

[14] J. Wang, H. Wong, Z. Ji, and Y. Wu, "Broadband CPW-fed aperture coupled metasurface antenna," *IEEE Antennas and Wireless Propagation Letters*, vol. 18, no. 3, pp. 517–520, 2019.

[15] B. Majumder, K. Krishnamoorthy, J. Mukherjee, and K. P. Ray, "Compact broadband directive slot antenna loaded with cavities and single and double layers of metasurfaces," *IEEE Transactions on Antennas and Propagation*, vol. 64, no. 11, pp. 4595–4606, 2016.

[16] C. Huang, C. J. Guo, Y. Yuan, and J. Ding, "Dual-band dual-sense high-gain circularly polarized metasurface antenna using characteristic mode analysis," *IEEE Antennas and Wireless Propagation Letters*, vol. 22, no. 1, pp. 154–158, 2023.

[17] H. H. Tran, C. D. Bui, N. Nguyen-Trong, and T. K. Nguyen, "A wideband non-uniform metasurface-based circularly polarized reconfigurable antenna," *IEEE Access*, vol. 9, pp. 42325–42332, 2021.

[18] R. F. Harrington and J. R. Mautz, "Theory of characteristic modes for conducting bodies," *IEEE Transactions on Antennas and Propagation*, vol. 19, no. 5, pp. 622–628, 1971.

[19] Y. K. Chen and C. F. Wang, *Characteristics Modes: Theory and Applications in Antenna Engineering*, Wiley, Hoboken, NJ, USA, 2015.

[20] B. B. Yang and J. J. Adams, "Computing and visualizing the input parameters of arbitrary planar antennas via eigenfunctions," *IEEE Transactions on Antennas and Propagation*, vol. 64, no. 7, pp. 2707–2718, 2016.

[21] R. F. Harrington, *Time-Harmonic Electromagnetic Fields*, McGraw-Hill, New York, NY, USA, 1961.

[22] G. Shaker, S. Safavi-Naeini, and N. Sangary, "Modern antenna design using mode analysis techniques," *Progress in Electromagnetics Research B*, vol. 62, pp. 153–165, 2015.

[23] E. B. Rosa, "The self and mutual inductances of linear conductors," *Bulletin of the Bureau of Standards*, vol. 4, no. 2, pp. 301–344, 1908.

[24] Y. P. Zhang, "Design and experiment on differentially-driven microstrip antennas," *IEEE Transactions on Antennas and Propagation*, vol. 55, no. 10, pp. 2701–2708, 2007.

[25] S. B. Park, S. M. Kim, and W. G. Yang, "Wideband circular polarization patch antenna for access point of 802.11B, G WLAN," *Microwave and Optical Technology Letters*, vol. 50, no. 4, pp. 1042–1046, 2008.

[26] M. Manteghi, "Analytical calculation of impedance matching for probe-fed microstrip patch antennas," *IEEE Transactions on Antennas and Propagation*, vol. 57, no. 12, pp. 3972–3975, 2009.

[27] P. Zhou, Y. Liu, H. Zhao, Y. Shi, and X. Yin, "Differentially fed dual-mode patch antenna with wideband common-mode absorption and its array application," *IEEE Transactions on Antennas and Propagation*, vol. 69, no. 12, pp. 8937–8942, 2021.

[28] Q. Xue, X. Y. Zhang, and C. H. K. Chin, "A novel differential-fed patch antenna," *IEEE Antennas and Wireless Propagation Letters*, vol. 5, pp. 471–474, 2006.